Available online at www.sciencedirect.com
ScienceDirect
Journal of the European Ceramic Society 30 (2010) 2547–2554
www.elsevier.com/locate/jeurceramsoc

Three-dimensional structure analysis by X-ray micro-computed tomography of macroporous alumina templated with expandable microspheres

Linnéa Andersson [a], Anthony C. Jones [b], Mark A. Knackstedt [b], Lennart Bergström [a,*]

[a] Department of Materials and Environmental Chemistry, Stockholm University, SE-10691 Stockholm, Sweden
[b] Department of Applied Mathematics, Research School of Physical Sciences and Engineering, Australian National University, Canberra, ACT 0200, Australia

Received 4 December 2009; received in revised form 23 April 2010; accepted 4 May 2010

Abstract

The three-dimensional (3D) structures of macroporous alumina, produced by a novel method that combines gel casting with expandable polymeric microspheres as a sacrificial templating material, have been characterised by X-ray micro-computed tomography (μ-CT). The grey-scale intensity tomogram data produced by the X-ray μ-CT was segmented into porous and solid phases and the individual pores were identified. We compared two-dimensional slices of the analysed data with the corresponding scanning electron microscopy images and showed that the structural features of the pores were well reproduced in the X-ray μ-CT images. 3D visualisations of the pore structure and the pore network were also shown. The open porosity obtained from X-ray μ-CT corresponded well with the porosity derived from mercury porosimetry for pores larger than the voxel dimension (3 μm). The quantitative analysis also yielded information on the spatial variations in porosity and the number of connected neighbours of pores. The 3D data was used to relate the calculated permeability to the open porosity.

Keywords: Porosity; X-ray methods; Non-destructive evaluation; Al_2O_3; Expandable microspheres

1. Introduction

Macroporous ceramics are established in a wide range of applications, such as diesel particulate filters,[1] catalyst supports,[2,3] and molten metal filters.[4] Porous inorganic materials are also promising candidates as bone scaffolds.[5,6] The properties of macroporous ceramics depend on the porous structure and the inherent materials properties of the chosen ceramic. The level of porosity, the type of porosity (open or closed) and the pore-size distribution are important characteristics of the porous structure. Other parameters such as the degree of connectivity between the pores, and the size of the pore openings (throat diameter) also have a strong effect on the pore phase accessibility and permeability to gas or fluid flow; structural features of importance for e.g. filtration and separation.[1,2,4]

The structure of macroporous ceramics is traditionally characterised by two-dimensional (2D) imaging or intrusion methods, such as mercury porosimetry. The imaging techniques include light microscopy and electron microscopy combined with image analysis or image reconstruction procedures.[3,7] Although these methods provide high resolution information on the local (surface) structure, the ability to extract statistically significant three-dimensional (3D) information of the bulk material is limited.[3] 3D information is particularly important in characterizing the connectivity, transport and accessibility properties of the porous solid. Confocal laser scanning microscopy (CLSM) is one non-destructive imaging technique which can in principle obtain and reconstruct 3D information, providing that the material is sufficiently transparent.[7] Even though the refractive index of most ceramic materials is too high for CLSM, it has been demonstrated that immersing fluids with similar dielectric properties as the solid can reduce scattering sufficiently to allow 3D information to be retrieved.[8,9] These restrictions significantly limit the use of CLSM for 3D characterisation.

X-ray micro-computed tomography (μ-CT) is a powerful non-destructive technique, which provides 3D information about heterogeneous materials. It has progressed from being a qualitative imaging technique used in medical science[7] to become a sophisticated structural analysis method in materials science.[10–13] The use of X-ray μ-CT is especially appropriate for the characterisation of porous materials, due to the distinct difference in the attenuation coefficient between the solid and

* Corresponding author. Tel.: +46 8 162368; fax: +46 8 152187.
E-mail address: lennart.bergstrom@mmk.su.se (L. Bergström).

0955-2219/$ – see front matter © 2010 Elsevier Ltd. All rights reserved.
doi:10.1016/j.jeurceramsoc.2010.05.003

gaseous (void) phases. A wide range of porous materials and cellular structures have been characterised with X-ray μ-CT: ceramics, concrete, metals, and various organic materials such as polymers, food stuff and materials for tissue engineering.[14–18]

A wide range of inherent 3D structural parameters that describe a porous structure can be analysed and quantitatively evaluated from 3D X-ray μ-CT data, such as volume fraction of the solid and pore phases, pore and throat-size distributions, wall thickness and the interconnectivity of the respective phases.[11,14,19] Studies have shown that quantified structural parameters derived from X-ray μ-CT data are in good agreement with other techniques, if the resolved length scale is smaller or equal to the important structural features of the material.[14,15,19]

Characterisation with X-ray μ-CT also offers a unique possibility to relate the material structure to processing conditions e.g. in foams of various compositions,[12,16,20,21] and to follow structural changes during mechanical testing and heat treatments.[10,13,22]

Macroscopic bulk properties, such as permeability, mechanical properties and conductivity, can be numerically simulated on the 3D data provided by the X-ray μ-CT.[14,23,24] Previous work has shown that the simulated results for different classes of porous material are in good agreement with experimental results.[23,25] Numerical simulations of fluid flow in a porous structure provide information on e.g. tortuosity, flow paths and interactions between multiphase fluids;[20,24–26] properties that are difficult to measure experimentally.

In this article we present a thorough structural analysis of macroporous alumina based on 3D imaging with X-ray μ-CT. The structures are presented both as 2D slices and 3D visualisations. The porous structure is evaluated qualitatively and compared with scanning electron microscopy images. The porosity and pore-size distribution are determined quantitatively and compared with results from mercury porosimetry. Information on the connected pore phase, and the number and sizes of the connections between the pores has been used to simulate the permeability at different porosities.

2. Experimental and numerical procedure

2.1. Procedure for making the macroporous alumina

The macroporous alumina was produced by gel casting a suspension of alumina, a monomer and cross-linker together with gas-filled microspheres. The microspheres expand upon heating and act as a templating material for the macropores. The monomer and cross-linker, which gel upon heating, preserve the porous structure created by the expanded microspheres. All organic materials were removed at an elevated temperature before pre-sintering the macroporous alumina at 1200 °C. The gel-casting process is described in detail in previous work.[27]

2.2. Starting materials

The alumina powder (AKP-30, Sumitomo Chemical Co., Ltd., Japan) has an average particle size (D_{50}) of 0.31 μm and was dispersed in the suspension with an ammonium polyacrylate (Darvan 821A, Vanderbilt Company Inc., USA). Methacrylic acid (MA) (Sigma–Aldrich Sweden AB, Sweden) and N,N′-methylenebisacrylamide (MBAM) (Sigma–Aldrich Sweden AB, Sweden) were used as the monomer and cross-linker, respectively. Ammonium persulfate (APS) (Sigma–Aldrich Sweden AB, Sweden) was used as the initiator for the radical polymerisation of the monomer and cross-linker.

The expandable polymeric microspheres (ON316WUX, Expancel, Sweden) consist of a co-polymer shell and are filled with a blowing agent (isobutane). The mean particle size (D_{50}) of the expandable microspheres is 33 μm in the unexpanded state.

2.3. Characterisation

2.3.1. X-ray micro-computed tomography

Image acquisition: the X-ray μ-CT instrument, operating with a cone beam geometry, was developed and built at the Australian National University.[28,29] The macroporous alumina materials were imaged with the X-ray source operating at 80 kV and with a beam current of 100 μA. A 1 mm thick dense aluminium filter was used to reduce the problem of beam hardening of the polychromatic beam, which may lead to artefacts in the radiographs.[28] A set of 2880 two-dimensional (2D) radiograph projections were acquired at different rotation angles covering the complete 360°. These radiographs were combined into 2048^3 voxel tomograms. The resulting voxel dimension of the tomograms was 3 μm.

Cylindrical samples with a diameter of 5 mm were extracted from the middle of macroporous alumina blocks to avoid edge effects from the mould. The acquisition times were approximately 15 h per sample.

Image reconstruction: the 2D radiographs are first pre-processed, which includes linearising the projection data and minimizing artefacts, and then reconstructed with a Feldkamp algorithm to generate a tomogram consisting of three-dimensional (3D) voxels.[28,30] Each resulting voxel has an intensity value relating to the X-ray attenuation at that specific point in the sample. The X-ray attenuation is non-linearly related to the density and the composition of the 3D volume represented by each voxel.[28]

2.3.2. Simulation of permeability to fluid flow

The permeability of the macroporous materials was calculated by using a lattice-Boltzmann (LB) method.[26] The LB approach is a mesoscopic numerical method used in computational fluid dynamics, where the macroscopic dynamics of the solution of a discretized Boltzmann equation can be shown to match the Navier–Stokes equation. Due to its simplicity in form and adaptability to complex flow geometries, like the presence of solid–fluid boundaries, one of the most successful applications of the LB method has been to simulate flow in complex porous media.[24,26] The simulations were conducted on independent sub-domains from each macroporous alumina data set with sizes varying between $(724)^3$ and $(1160)^3$ μm^3. The sub-volumes have dimension larger than 10 times the mean pore size, which has been shown to be sufficient for accurate simulation of permeability.[23,25]

Table 1
Characteristics of the macroporous alumina materials.

Material[a]	Amount of expandable microspheres (wt% DWB)[b]	Porosity (%)		Mean pore diameter with standard deviation [σ] (μm)[c]		Mean number connected pore neighbours with standard deviation [σ][c]	
		μ-CT	Hg	By number	By volume	By number	By volume
MA-EPS-76	1.8	75.5	82.8	60 [52]	180 [84]	3 [5]	16 [14]
MA-EPS-57	1.1	57.1	72.8	74 [50]	196 [98]	5 [4]	17 [18]
MA-EPS-51	0.7	51.1	67.3	72 [48]	200 [98]	2 [3]	12 [12]
MA-EPS-46	0.3	46.1	64.6	60 [52]	240 [134]	1 [3]	14 [18]

[a] The MA-EPS-number refers to the level of porosity in the sample as determined by X-ray μ-CT. MA and EPS is short for macroporous alumina and expandable polymeric spheres, respectively.
[b] The amount of sacrificial templating material in suspension, in wt% dry weight basis (DWB).
[c] The mean value is weighted by the number of pores or by the volume of the pores.

The permeability of each sub-volume was calculated by applying a simulated pressure gradient to the liquid in one direction.[24] The outer boundaries of the simulated domain, perpendicular to the pressure gradient, were covered by a layer of fluid.[25] At solid–fluid interfaces the physical boundary condition is the no-flow condition.[26] The presented permeability values are the restriction of the permeability tensors to the direction of the pressure gradient.

2.3.3. Scanning electron microscopy

The scanning electron microscopy (SEM) was performed with a Zeiss UltraPlus analytical FESEM at an acceleration voltage of 20 kV.

2.3.4. Mercury porosimetry

The porosity and pore diameter of the porous alumina were evaluated by mercury intrusion porosimetry (Micromeritics AutoPore III 9410), assuming a surface tension and contact angle of mercury of 485 mN/m and 130°, respectively.

3. Results and discussion

The three-dimensional (3D) structures of macroporous alumina materials, with average porosities ranging between 46 vol% and 76 vol%, were analysed with X-ray micro-computed tomography (μ-CT). These materials were produced by a recently developed method that combines gel casting with expandable polymeric microspheres (EPS) as a sacrificial templating material.[27] Table 1 presents the characteristics of the materials.

The analysis of grey-scale X-ray μ-CT tomograms of porous and composite materials is a challenge since features at or below the instrument resolution will blur sharp edges at phase boundaries. Therefore the tomogram data, which is presented in grey levels corresponding to the X-ray attenuation, is treated with image enhancing filters to reduce noise and blur. We used two different filters in sequence: a denoising anisotropic diffusion filter and an edge sharpening "unsharp mask" filter.[31]

It should be noted that all organic additives were removed and the materials were presintered prior to the structural characterisation. Hence, the macroporous materials only contain two phases: alumina and air. The voxel intensity histogram in Fig. 1(a) shows that it is possible to identify two distinctive peaks that represent the two phases. For further analysis, the voxelated data need to be categorised as either solid or void; this process is called segmentation. In this work the segmentation was performed with a method known as "converging active contours", which is a combination of a watershed transform and the active contour method.[31] This approach is based on user-defined "seeding regions" for each phase. Two cut-off values close to the intensity peaks were selected; everything below the lower limit is designated as pore and everything above the upper limit is designated as solid (Fig. 1(a)). The intensity values between these cut-off boundaries were assigned to each binary phase by the converging active contour method. Fig. 1((b) and (c)) shows a comparison of a grey-scale tomogram slice with the binarised result after segmentation. We chose cut-off boundaries that

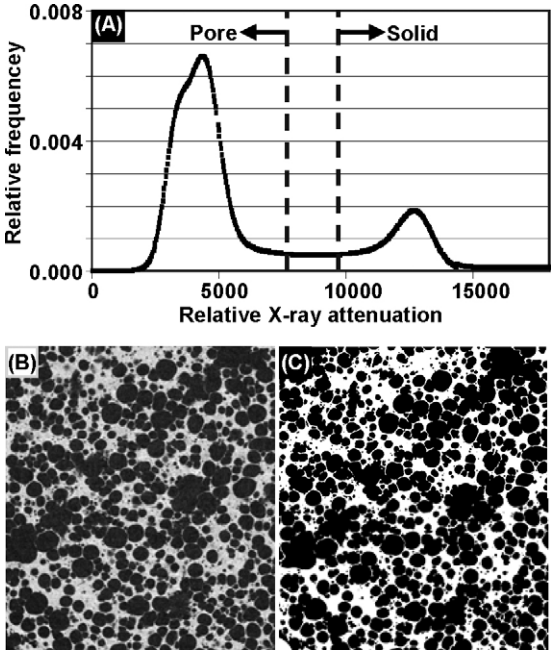

Fig. 1. X-ray μ-CT intensity histogram and grey-scale and binarised 2D representations. In (a) the intensity histogram of the entire tomogram shows a significant difference in X-ray attenuation between the two phases: pore (left peak) and solid (right peak). The cut-off values for the segmentation seeding regions of the two phases are indicated by the dotted lines in (a). A reconstructed grey scale tomogram slice is shown in (b). The binarised result after segmentation is shown in (c) where white represents the solid (Al_2O_3) and black the porous phase, respectively.

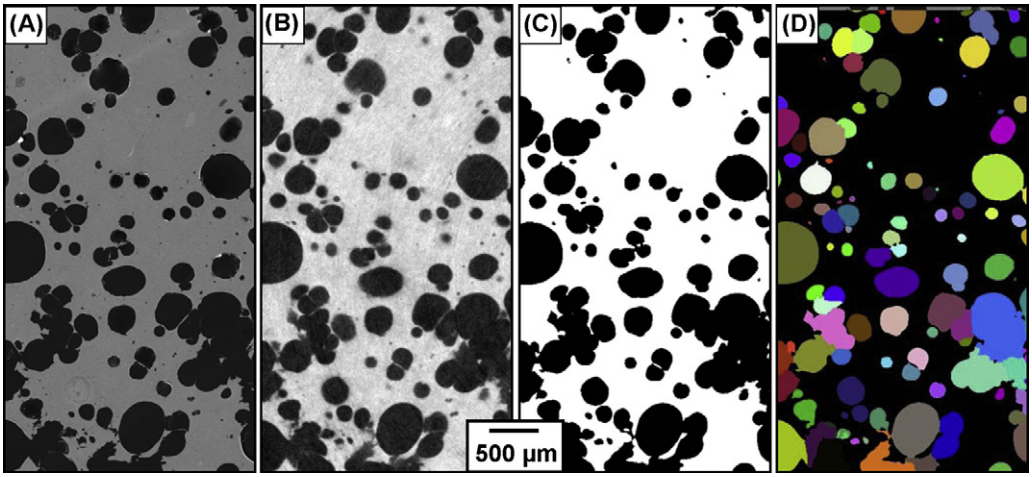

Fig. 2. Comparison between a SEM image and 2D X-ray μ-CT representations of a macroporous alumina with an average porosity of 51 vol%. In (a) the SEM image, which can be compared with the corresponding X-ray μ-CT data at different stages of the analysis: (b) the grey-scale tomogram, (c) the binarised data after segmentation and (d) after identification of the individual pores.

optimised the reconstruction of the shape of the overall porous structure, maintaining a focus on capturing thin pore walls.

We used scanning electron microscopy (SEM) to qualitatively evaluate the limits of the X-ray μ-CT method to accurately capture the morphological features of the porous materials. Fig. 2 shows a comparison of an SEM image with two-dimensional (2D) slices from different stages in the treatment of the X-ray μ-CT data. The data was selected from the same position from a macroporous alumina material with an average porosity of 51 vol%. An algorithm aligned the SEM image to identify the corresponding 2D slice in the 3D data-sets of the grey-scale tomogram and segmented data.[32] We found that the shape of the pores was very well reproduced in the segmented X-ray μ-CT image, whereas the fine features of e.g. some pore walls could not be captured in detail.

Pore walls of 1–3 voxels width (i.e. 3–9 μm) could not be entirely captured in the segmentation without over-exaggerating the whole solid phase. This is due to the low intensity gradients between the solid and porous phase and the resolution of X-ray μ-CT tomogram which is 3 μm. These effects related to the appearance of incomplete pore walls after segmentation (Fig. 2(a)–(c)). Similarly, singular pores smaller than 10 voxels (30 μm) could sometimes not be resolved in the dataset, which is seen when the tomogram is compared to the segmented data in Fig. 2(b) and (c), respectively. It should be noted, however, that even if these small sized pores with thin pore walls could not be entirely captured in a single 2D plane (slice), parts of these structures may be captured in the corresponding 3D data set.

The next step in the 3D analysis is to identify the pores and the pore throats in the segmented data. This is necessary before a quantitative analysis on the characteristics and properties of the porous material can be performed. The identification was based on an Euclidean distance map, in which each pore voxel's distance to the nearest solid phase is calculated.[33] A watershed function, applied to this distance map, partitions the pore space into pore bodies. To identify distinct pores, seed regions of the watershed are introduced at the centres of the pore bodies and allowed to grow until they encounter another growing pore region.[29,33] A pore merging algorithm is applied to the partitioned pore space to reduce any over-partitioning. As the watershed algorithm considers the 3D structural information of a pore space, it can divide a large porous region into several distinct pores. Fig. 2(d) shows a 2D slice of the pore structure in which the pores are identified and individually coloured.

Once the data has been processed to identify distinct pores, a network model can be created, which allows the 3D connectivity and pore/throat characteristics of the material to be defined. The pore throats, which are the open connections between the pores, are identified and as a result the pores are divided into sub-volumes separated at their narrowest constrictions.[29,33,34] Thereafter, a pore network is generated using a refined medial axis transform.[33,35,36]

Two different methods to visualise the 3D data-sets are illustrated in Fig. 3. Fig. 3(a) and (c) show segmented volume visualisations of two different macroporous alumina materials; the schematic stick-and-ball illustrations in Fig. 3(b) and (d) are the respective representations of the connected pore network. In this schematic, pores are shown as spheres while throats are represented by cylinders. The centre of the sphere corresponds to the centre of geometry of the pore, while the diameter is proportional to the diameter of the largest sphere that can be inscribed within the pore.[11,36] The diameter of the cylinders correspond to the diameter of the throats. The number of cylinders connected to each sphere also illustrates the number of connected pore neighbours. The network models are visualised using Drishti, a volume visualisation program developed at the Australian National University.[29,37] Note that the geometric representations in Fig. 3(b) and (d) only are schematic illustrations of the network topology; the throats are e.g. pictured as straight cylinders, even if that is not the case in reality.

We calculated the pore-size distributions from the 3D data-sets for the macroporous alumina materials. The pore-size distribution of macroporous alumina with an average porosity of 76 vol% (MA-EPS-76) is presented in Fig. 4. The number-based pore-size distribution (Fig. 4) displays two peaks: one peak at 6 μm and one peak at 40 μm. The volume-based pore-size

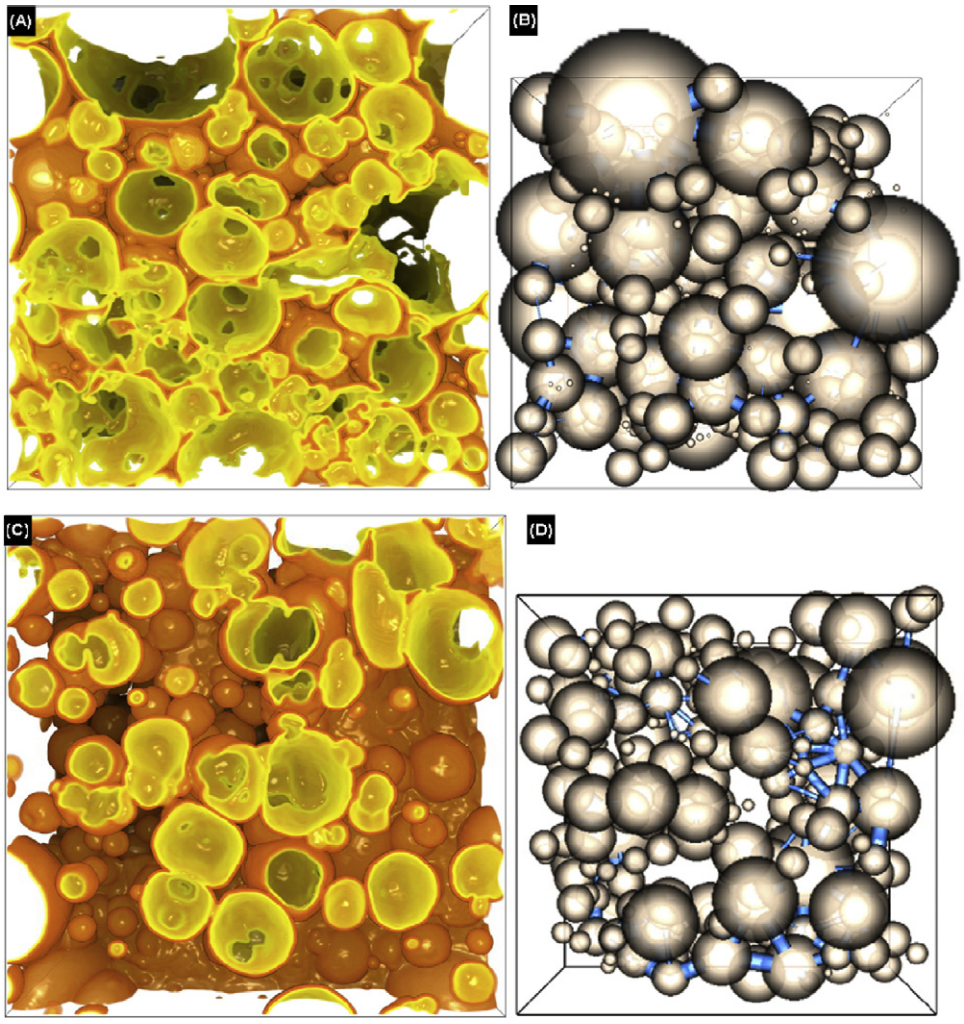

Fig. 3. Three-dimensional representations of macroporous alumina materials with an average porosity of 76 vol% (a and b) and 51 vol% (c and d). In (a) and (c) the representations are based on segmented data. The surface of the pores is highlighted with a yellow colour, whereas the solid phase in orange is slightly transparent to increase visibility. In (b) and (d) three-dimensional network model images show how the pores, here pictured as spheres, are connected by throats, represented by cylinders. The data sets are 1160 μm × 1160 μm × 580 μm in size. (For interpretation of the references to color in this figure legend, the reader is referred to the web version of this article.)

distribution in Fig. 4 only displays one peak at 60 μm, which reflects the influence of pores with a large volume. Indeed, Table 1 shows that the volume-based mean pore size is 3–4 times larger than the number-based mean pore-size distribution for all the investigated materials. This demonstrates that the pore-size distribution is relatively broad with pore sizes ranging from below 10 μm up to about 200 μm. The pore-size distributions were derived by applying a maximum covering sphere (MCS) algorithm on the segmented data of the macroporous alumina.[33,36,38] The pore-size distributions reflect the diameter of a MCS inscribed at each voxel of the porous phase.

We have also determined the total porosity and identified and quantified the open (connected) porosity from the segmented X-ray μ-CT datasets. The porosity is determined by counting the number of voxels in the void phase in the segmented data set and normalising that to the total number of voxels. Table 1 shows that the total porosity obtained from X-ray μ-CT is significantly smaller than the porosity determined by mercury porosimetry. This is not surprising considering the large difference in the detection limit of the different techniques; mercury porosimetry has a lower detection limit around 10 nm while the detection limit of X-ray μ-CT is mainly determined by the resolution.

Fig. 5 shows that the mercury porosimetry porosity determined from pores equal to and larger than the voxel resolution (3 μm) correlates very well with the open porosity determined from X-ray μ-CT. The correlation between the X-ray μ-CT and mercury porosimetry data holds over a porosity range between 40 vol% and 80 vol%, in which the open porosity is found to depend linearly on the amount of expandable spheres added to the gel-casting suspension. The open porosity is derived by removing the pores which are connected neither to the percolating pore phase nor to the outer surface.

The 3D structural information has also been used to evaluate spatial porosity variations in the macroporous bodies. Fig. 6 shows how the porosity varies in the z-direction, which corresponds to the direction perpendicular to the bottom of the mould. We find that the spatial variation is significantly smaller for the highest porosity (76%) macroporous alumina templated with

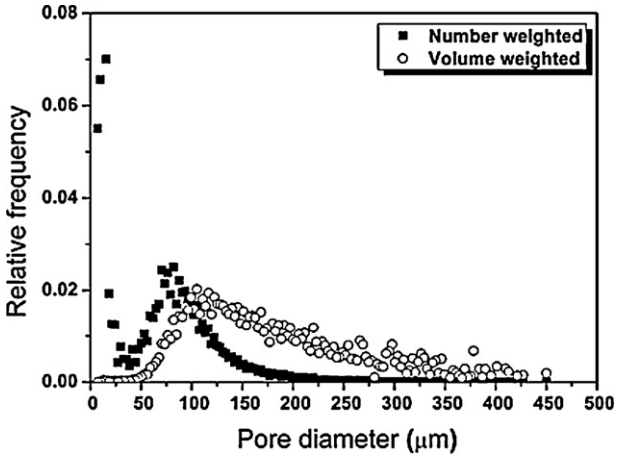

Fig. 4. The pore-size distribution for macroporous alumina with an average porosity of 76 vol%. The pore-size distribution is derived with a maximum covering sphere (MCS) algorithm from the segmented data. The pore diameter distribution is presented both weighted by volume and weighted by number. The mean pore diameter for each macroporous alumina material is shown in Table 1.

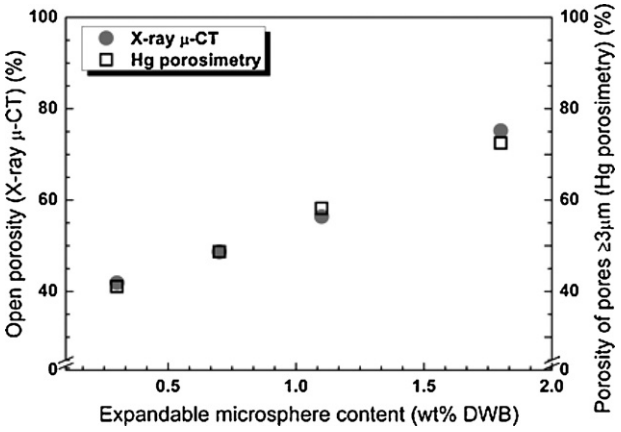

Fig. 5. Comparison of the open porosity from the X-ray μ-CT with the porosity from pores of diameter ≥3 μm from the mercury (Hg) porosimetry at different amounts of added expandable microspheres on a dry weight basis (DWB).

EPS (MA-EPS-76), compared to the lowest porosity (46–57%) macroporous alumina templated with EPS (MA-EPS-46, MA-EPS-51, and MA-EPS-57).

The 2D slices in Fig. 6 show that the regions with maximum porosity in the low-porosity materials (MA-EPS-46 and MA-EPS-51) contain much larger pores and a more inhomogeneous distribution of the solid phase and the pores compared to the high-porosity materials (MA-EPS-76). We speculate that the expandable spheres are able to expand more when a relatively low amount is added compared to high additions when crowding will restrict the expansion. Indeed, the data in Table 1 also show that the volume-based mean pore size increases with decreasing amount of expandable spheres added.

We have also used the segmented 3D data to estimate the permeability of the macroporous alumina. Fig. 7 shows the permeability of macroporous alumina materials with porosities ranging from 36 to 83 vol%. The permeability to fluid flow was calculated by simulating a pressure gradient in one direction: the y-direction. In Fig. 7 the permeability κ_{yy} represents the permeability in the same direction as the simulated pressure gradient.

The simulated permeability is reported in units of microns squared as a function of the connected porosity in the subvolumes. The units are defined as an areal measure since the permeability of a porous medium is limited by the effective channel cross-sectional area available for fluid flow. It thus depends on the area of the constrictions in the pore phase.[34]

The data in Fig. 7 displays the expected trend of increasing permeability with an increase in the connected porosity (Table 1). However, the scatter is significant and the simulations show that the permeability fluctuates more in the macroporous alumina materials at lower porosities compared to the materials at porosities above 60% (Fig. 7). This difference in permeability

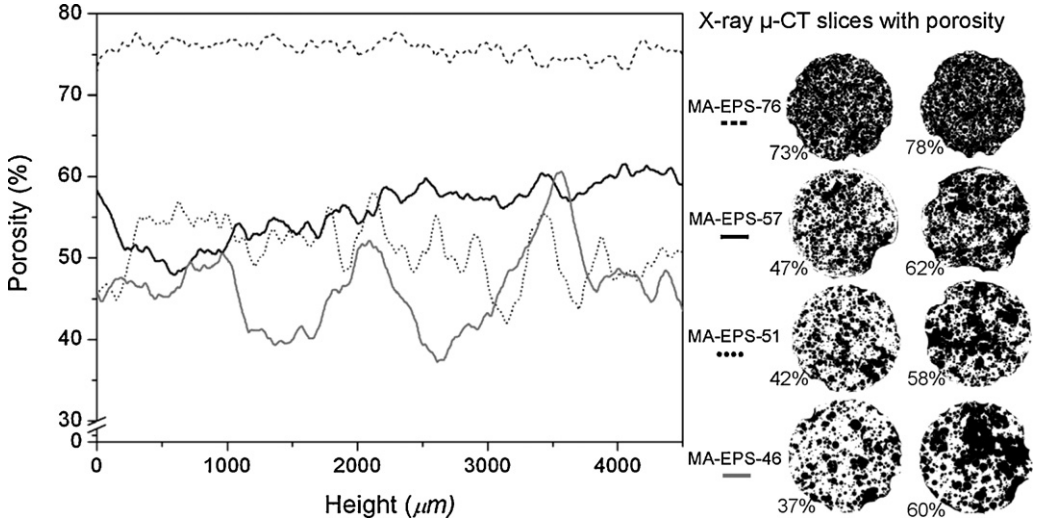

Fig. 6. Spatial porosity fluctuation in the z-direction of macroporous alumina materials with an average porosity of 76 vol%, 57 vol%, 51 vol% and 46 vol%, respectively. The profile of the pore phase fraction in the segmented 3D data is plotted as a function of height, and is matched with 2D images, on the right hand side, that display slices with maximum and minimum porosities for each material. In the 2D images white represents the solid phase and black represents the porous phase (void).

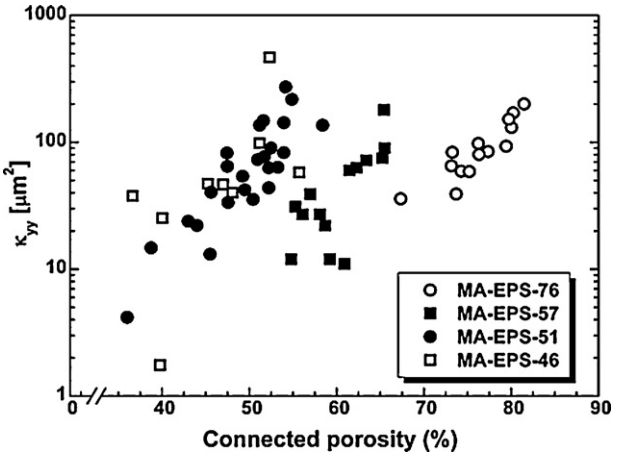

Fig. 7. Simulated permeability in the *y*-direction of macroporous alumina materials plotted as a function of connected porosity. Each data point results from a sub-volume of $(724)^3$–$(1160)^3$ μm^3.

variations with porosity may be related to the observed spatial variations in porosity shown in Fig. 6.

4. Conclusions

We have determined the three-dimensional (3D) structure of macroporous alumina materials by a combination of X-ray micro-computed tomography (X-ray μ-CT), mercury porosimetry and scanning electron microscopy (SEM). The materials were produced by a novel method that combines gel casting with expandable polymeric microspheres (EPS) as a sacrificial templating material. The average porosities in these materials ranged between 46% and 76%.

We have shown that the binarisation of the original grey-scale X-ray μ-CT data using the "converging active contours" segmentation method is able to capture the details of the porous and solid phases. This was confirmed by comparing a SEM image of a cross-sectional cut of the material with the corresponding cross-section of the segmented 3D data. We also demonstrated, with an extension of these methods, the identification of individual pores. The macroporous alumina materials were visualised with 3D representations of the segmented data and the corresponding pore-network models.

The pore-size distributions were determined and both number-based and volume-based distributions were shown. These distributions suggest that the pore sizes of the macroporous alumina produced by using EPS as a sacrificial template is relative wide (3–450 μm). The open porosity obtained from the X-ray μ-CT was in excellent agreement with the porosity obtained from mercury porosimetry of pores larger than the X-ray μ-CT resolution (3 μm). The detailed information on the pore connectivity and percolation enabled the permeability of the macroporous alumina to be calculated using a lattice-Boltzmann method.

Acknowledgements

The Swedish Research Council (VR) and the Berzelii center EXSELENT on porous materials are acknowledged for funding. L. Andersson wishes to thank the Swedish Chemical Society and Knut and Alice Wallenberg foundation for travel grants. The ANU Electron Microscopy Unit is acknowledged for the use of the Zeiss UltraPlus analytical FESEM. Ph.D. Michael Turner, Jill Middleton, Bianka Malzacher and Ph.D. Shane Latham at the ANU are thanked for help with 3D imaging and data analysis. Ph.D. Christopher Arns is recognised for assistance with the permeability simulation.

Appendix A. Supplementary data

Supplementary data associated with this article can be found, in the online version, at doi:10.1016/j.jeurceramsoc.2010.05.003.

References

1. Adler J. Ceramic diesel particulate filters. *Int J Appl Ceram Technol* 2005;**2**:429–39.
2. Richardson JT, Peng Y, Remue D. Properties of ceramic foam catalyst supports: pressure drop. *Appl Catal* 2000;**204**:19–32.
3. Scheffler M, Colombo P. Cellular ceramics: structure, manufacturing. In: *Properties and applications.* Weinheim: Wiley-VCH; 2005, 645 p.
4. Gauckler LJ, Waeber MM, Conti C, Jacob-Dulière M. Industrial application of open ceramic foam for molten metal filtration. *Light Met* 1985:1261–83.
5. Hench LL. *Bioceram J Am Ceram Soc* 1998;**81**:1705–28.
6. Hutmacher DW. Scaffolds in tissue engineering bone and cartilage. *Biomaterials* 2000;**21**:2529–43.
7. Clarke AR, Eberhardt CN. *Microscopy techniques for materials science*. Cambridge, England: Woodhead Publishing Limited; 2002, 424 p.
8. Uchida N, Bergstrom L. Quantification of the internal structure in ceramic green bodies using computer-assisted optical imaging. *J Eur Ceram Soc* 1997;**17**:1193–200.
9. Ren F, Smith IO, Baumann MJ, Case ED. Three-dimensional microstructural characterization of porous hydroxyapatite using confocal laser scanning microscopy. *Int J Appl Ceram Technol* 2005;**2**:200–11.
10. Baruchel J, Buffiere J, Cloetens P, Di Michiel M, Ferrie E, Ludwig W, et al. Advances in synchrotron radiation microtomography. *Scripta Mater* 2006;**55**:41–6.
11. Sakellariou A, Arns CH, Sheppard AP, Sok RM, Averdunk H, Limaye A, et al. Developing a virtual materials laboratory. *Mater Today* 2007;**10**:44–51.
12. Blacher S, Léonard A, Heinrichs B, Tcherkassova N, Ferauche F, Crine M, et al. Image analysis of X-ray microtomograms of Pd–Ag/SiO_2 xerogel catalysts supported on Al_2O_3 foams. *Colloid Surf A* 2004;**241**:201–6.
13. Salvo L, Cloetens P, Maire E, Zabler S, Blandin JJ, Buffière JY, et al. X-ray micro-tomography an attractive characterisation technique in materials science. *Nucl Instrum Methods B* 2003;**200**:273–86.
14. Maire E, Fazekas A, Salvo L, Dendievel R, Youssef S, Cloetens P, et al. X-ray tomography applied to the characterization of cellular materials. Related finite element modeling problems. *Compos Sci Technol* 2003;**63**:2431–43.
15. Maire E, Colombo P, Adrien J, Babout L, Biasetto L. Characterization of the morphology of cellular ceramics by 3D image processing of X-ray tomography. *J Eur Ceram Soc* 2007;**27**:1973–81.
16. Babin P, Della Valle G, Dendievel R, Lourdin D, Salvo L. X-ray tomography study of the cellular structure of extruded starches and its relations with expansion phenomenon and foam mechanical properties. *Carbohydr Polym* 2007;**68**:329–40.
17. Jones AC, Arns CH, Sheppard AP, Hutmacher DW, Milthorpe BK, Knackstedt MA. Assessment of bone ingrowth into porous biomaterials using MICRO-CT. *Biomaterials* 2007;**28**:2491–504.
18. Ho ST, Hutmacher DW. A comparison of micro CT with other techniques used in the characterization of scaffolds. *Biomaterials* 2006;**27**:1362–76.
19. Al-Raoush RI, Willson CS. Extraction of physically realistic pore network properties from three-dimensional synchrotron X-ray microtomography

images of unconsolidated porous media systems. *J Hydrol* 2005;**300**: 44–64.
20. Knackstedt MA, Arns CH, Saadatfar M, Senden TJ, Limaye A, Sakellariou A, et al. Elastic and transport properties of cellular solids derived from three-dimensional tomographic images. *Proc R Soc A* 2006;**462**:2833–62.
21. Lambert J, Cantat I, Delannay R, Mokso R, Cloetens P, Glazier JA, et al. Experimental growth law for bubbles in a moderately "Wet" 3D liquid foam. *Phys Rev Lett* 2007;**99**:058304.
22. Elliott JA, Windle AH, Hobdell JR, Eeckhaut G, Oldman RJ, Ludwig W, et al. In-situ deformation of an open-cell flexible polyurethane foam characterised by 3D computed microtomography. *J Mater Sci* 2002;**37**:1547–55.
23. Arns CH, Knackstedt MA, Pinczewski MV, Lindquist WB. Accurate estimation of transport properties from microtomographic images. *Geophys Res Lett* 2001;**28**:3361–4.
24. Ferréol B, Rothman DH. Lattice-Boltzmann simulations of flow through Fontainebleau sandstone. *Transp Porous Media* 1995;**20**:3–20.
25. Arns CH, Knackstedt MA, Pinczewski WV, Martys NS. Virtual permeametry on microtomographic images. *J Petrol Sci Eng* 2004;**45**:41–6.
26. Martys NS, Chen H. Simulation of multicomponent fluids in complex three-dimensional geometries by the lattice-Boltzmann method. *Phys Rev E* 1996;**53**:743–50.
27. Andersson L, Bergström L. Gas-filled microspheres as an expandable sacrificial template for direct casting of complex-shaped macroporous ceramics. *J Eur Ceram Soc* 2008;**28**:2815–21.
28. Sakellariou A, Sawkins TJ, Senden TJ, Limaye A. X-ray tomography for mesoscale physics applications. *Phys A* 2004;**339**:152–8.
29. Sheppard AP, Arns CH, Sakellariou A, Senden TJ, Sok RM, Averdunk H, et al. Quantitative properties of complex porous materials calculated from X-ray μ-CT images. In: *Developments in X-ray Tomography V Proceedings of SPIE*. 2006.
30. Feldkamp LA, Davis LC, Kress JW. Practical cone-beam algorithm. *J Opt Soc Am A* 1984;**1**:612–9.
31. Sheppard AP, Sok RM, Averdunk H. Techniques for image enhancement and segmentation of tomographic images of porous materials. *Phys A* 2004;**339**:145–51.
32. Latham SJ, Varslot TK, Sheppard AP. Automated registration for augmenting micro-CT 3D images. *ANZIAM J* 2008;**50**:C534–48.
33. Sheppard AP, Sok RM, Averdunk H. Improved pore network extraction methods. In: *In 19th International Symposium of the Society of Core Analysts*. 2005. p. 1–11.
34. Lindquist WB, Venkatarangan AB, Dunsmuir JH, Wong TF. Pore and throat size distributions measured from synchrotron X-ray tomographic images of Fontainebleau sandstones. *J Geophys Res* 2000;**105B**:21508–28.
35. Lindquist WB, Lee SM, Coker DA, Jones JW, Spanne P. Medial axis analysis of void structure in three-dimensional tomographic images of porous media. *J Geophys Res* 1996;**101B**:8297–310.
36. Silin D, Patzek T. Robust determination of the pore space morphology in sedimentary rocks. In: *SPE 84296*. 2003. p. 1–15.
37. Limaye A. *Drishti—volume exploration and presentation tool*; 2006.
38. Delerue JF, Perrier E, Yu ZY, Velde B. New algorithms in 3D image analysis and their application to the measurement of a spatialized pore size distribution in soils. *Phys Chem Earth Pt A* 1999;**24**:639–44.